Cyclable Manganese Inventory as a Mechanistic Descriptor for Electrolyte Design in Rechargeable Aqueous Zn–MnO2 Batteries

Binglin Li[1]; Chen Wang[1]; Dongxv Guo[1]；Wanyi Wang[1]; Chenlin Sun[1], Shenghan Wang[1,*]

[1]Key Laboratory of Physics and Technology for Advanced Batteries (Ministry of Education), College of Physics, Jilin University, Changchun 130012, China

E-mails:shenghan@jlu.edu.cn

Experimental Section

Electrode Preparation and Battery Assembly

β-MnO_2, Super-P conductive carbon black, and PVDF binder were mixed in a mass ratio of 7:2:1 in N-methylpyrrolidone (NMP) and ground to form a homogeneous slurry, which was then coated onto a stainless steel current collector. The electrode was dried under vacuum at 80 °C for 12 h, pressed, and cut into disks with a diameter of 12 mm. CR2032 coin cells were assembled using a zinc foil as the anode, a glass fiber membrane (Whatman GF/D) as the separator, and 100 μL of freshly prepared electrolyte.

Materials Characterization and Electrochemical Testing

Materials characterization: Electrode morphologies were observed using scanning electron microscopy (SEM, Hitachi SU8010). Phase analysis was performed using X-ray diffraction (XRD, Bruker D8 Advance).

Electrochemical testing: Galvanostatic charge–discharge tests were conducted using a LAND CT2001A testing system within a voltage range of 0.9–1.8 V. Mn^{2+} electrodeposition behavior was investigated using a MnO_2-free electrodeposition configuration under a constant current of 0.1 mA. In this test, a bare Ti foil was used as the cathode-side substrate to collect the electrodeposited Mn-containing species, while Zn foil was used as the anode. The cell was assembled in a CR2025-type coin cell configuration using 316L stainless-steel positive and negative cases, a spacer with a diameter/thickness of 15.8 mm/0.5 mm, and a spring with a diameter/thickness of 15.4 mm/1.1 mm. This configuration was designed to directly evaluate the Mn^{2+} deposition behavior in different electrolytes without the influence of a pre-existing MnO_2 cathode .The initial pH of the electrolytes was measured using a pH meter.

Materials and Chemical Reagents

All chemical reagents used in the experiments were of analytical grade and were used without further purification. Deionized water was used to prepare all electrolytes. Detailed information on the materials and reagents is provided in Table S1.

Table S1 Experimental materials and chemical reagents

Material/Reagent Name	Chemical Formula/Abbreviation	Specification	Manufacturer
Manganese dioxide	β-MnO_2	Battery grade	Aladdin
Zinc foil	Zn	Thickness 0.1 mm, purity 99.99%	Alfa Aesar
Conductive carbon black	Super-P	Battery grade	Timcal
Polyvinylidene fluoride	PVDF	Battery grade	Xiya Reagent
N-Methylpyrrolidone	NMP	Analytical grade	Macklin
Zinc sulfate	$ZnSO_4·7H_2O$	Analytical grade	Aladdin
Zinc acetate	$Zn(CH_3COO)_2·2H_2O$	Analytical grade	Aladdin
Manganese sulfate	$MnSO_4·H_2O$	Analytical grade	Aladdin

Manganese acetate	$Mn(CH_3COO)_2 \cdot 4H_2O$	Analytical grade	Aladdin
Citric acid	$C_6H_8O_7$	Analytical grade	Sinopharm Group
Glass fiber separator	GF/D	Whatman	Fushun Filter Paper Factory

Voltage Plateau Analysis Based on the Nernst Equation

To thermodynamically validate the proton consumption effect of acetate ions (CH_3COO^-), a theoretical analysis of the initial discharge voltage plateaus was cond ucted using electrolytes with varying acetate concentrations. The analysis is based on the overall reaction of the aqueous Zn–MnO_2 battery (Eq. S1) and the corresponding Nernst equation (Eq. S2).

I. Reaction Equations and Simplification of the Nernst Equation

Overall reaction:

$$MnO_2 + Zn + 4H^+ \rightarrow Mn^{2+} + Zn^{2+} + 2H_2O \quad (S1)$$

Standard electromotive force:

$E^\circ = \varphi^\circ(MnO_2/Mn^{2+}) - \varphi^\circ(Zn^{2+}/Zn) = 1.99\ V$

The actual electromotive force (E) is given by the Nernst equation:

$$E = E^\circ - \frac{0.059}{2} log \frac{[Mn^{2+}][Zn^{2+}]}{[H^+]^4} \quad (S2)$$

To highlight the effect of acetate ions on proton concentration, the following simplifications were applied. During the initial discharge plateau, the activities of Mn^{2+} and Zn^{2+} are assumed to be comparable, and their influence on the voltage is negligible relative to that of the proton concentration. Thus, Mn^{2+}=Zn^{2+}=1M was taken as the reference. Substituting this assumption into Eq. (S2) yields:

$$E = 1.99 - 0.0296 log \frac{1}{[H^+]^4} \quad (S3)$$

This equation indicates that the discharge voltage plateau (E) is directly dependent on the proton concentration ($[H^+]$) of the electrolyte.

II. Estimation of the Effect of Acetate Ions on [H^+]

The $[H^+]$ in the electrolyte is governed by the hydrolysis equilibria of Zn^{2+} and CH_3COO^-. Zn^{2+} and CH_3COO^- undergo double hydrolysis in a 1:2 stoichiometric ratio:

$$Zn^{2+} + 2CH_3COO^- + 2H_2O \rightleftharpoons Zn(OH)_2 + 2CH_3COOH \quad (S4)$$

This reaction consumes a portion of Zn^{2+} and CH_3COO^-, and the products do not contribute H^+ or OH^-. If Zn^{2+} remains after double hydrolysis, it undergoes further single-step hydrolysis (only the first step is consideredas $K_{h1} \gg K_{h2}$:

$$Zn^{2+} + H_2O \rightleftharpoons Zn(OH)^+ + H^+, K_h = 2.5 \times 10^{-10} \quad (S5)$$

To simplify the calculation, we assume that $Zn(OH)^+$ and H^+ are equivalent. Then, the hydrolysis constant can be approximated as:

$$K_h \approx \frac{[H^+]^2}{[Zn^{2+}]} \quad (S6)$$

Thus, the $[H^+]$ derived from the remaining Zn^{2+} concentration is:

$$[H^+] = \sqrt{K_h \cdot [Zn^{2+}]_{ex}} \quad (S7)$$

Based on the electrolyte composition, the amount consumed by double hydrolysis was first subtracted, and the $[H^+]$ generated from the hydrolysis of the remaining Zn^{2+} was calculated using Eq. (S7). For the pure $Zn(CH_3COO)_2$ system, the double hydrolysis consumes most of the Zn^{2+} and Ac^-; the

pH was experimentally measured to be approximately 6.0 (between the theoretical pH of 7 for complete double hydrolysis and the actual incomplete hydrolysis), so pH = 6.0 was used for the calculation.

III. Results and Comparison with Experiment

Table S2 summarizes the calculated [H^+], pH, and theoretical electromotive force E derived from Eq. (S3) for the five electrolyte systems.

Table S2 Calculated proton concentration, pH, and theoretical electromotive force E for differentelectrolyte systems

Zn^{2+}:CH_3COO^- Ratio	**[H^+] Calculation Process**	**pH**	**E(V)**
Pure $ZnSO_4$	$[H^+] = 1.58 \times 10^{-5}$ M	4.80	1.422
0.75:0.25	$[H^+] = 37 \times 10^{-5}$ M	4.86	1.414
0.5:0.5	$[H^+] = 12 \times 10^{-5}$ M	4.95	1.404
0.25:0.75	$[H^+] = 0.79 \times 10^{-5}$ M	5.10	1.386
Pure $Zn(CH_3COO)_2$	Experimental pH ≈ 6.0 (corresponding to) $[H^+] \approx 1.0 \times 10^{-6}$ M	6.00	1.280

IV. Conclusion

The calculations demonstrate that as the proportion of acetate ions increases, the effective [H^+] decreases continuously, accompanied by a corresponding increase in pH, resulting in a systematic decrease in the theoretical discharge voltage (E). This trend is in complete agreement with the experimentally observed decrease in the discharge plateau (Fig. 2(c)). Thus, the analysis thermodynamically confirms that the introduction of acetate ions (CH_3COO^-) significantly consumes protons, reducing the effective proton concentration of the electrolyte and consequently diminishing the thermodynamic driving force

100-Cycle-Averaged Estimation of the Apparent Cyclable Manganese Inventory

To semi-quantitatively compare the amount of manganese involved in reversible cycling in different electrolyte systems, the discharge capacities over the first 100 cycles were averaged and converted into a 100-cycle-averaged capacity-derived apparent cyclable Mn inventory. This analysis is based on the MnO_2/Mn^{2+} conversion reaction and Faraday's law. It should be noted that the calculated value represents a Mn-equivalent electrochemical estimate derived from discharge capacity, rather than a direct measurement of the actual manganese inventory.

I. Reaction Equation

The discharge process associated with MnO_2 reduction can be described as:

$$MnO_2 + 4H^+ + 2e^- \rightarrow Mn^{2+} + 2H_2O \quad \text{(S8)}$$

Correspondingly, during charging, Mn^{2+} is oxidized and electrodeposited as MnO_2. Therefore, one mole of manganese participating in the MnO_2/Mn^{2+} conversion corresponds to the transfer of two moles of electrons.

In principle, the reversible capacity of a given cycle should be taken as the smaller value between the charge and discharge capacities:

$$Q_{\mathrm{rev},i} = min(Q_{ch,i}, Q_{\mathrm{dis},i}) \quad \text{(S9)}$$

where $Q_{ch,i}$ and $Q_{dis,i}$ are the charge and discharge capacities of the i-th cycle, respectively. In the present work, the Coulombic efficiencies during the first 100 cycles are close to 100%, indicating that $Q_{ch,i}$ and $Q_{dis,i}$ are nearly identical for each cycle. Therefore, the discharge capacity of each cycle was used as a reasonable approximation of the reversible capacity of that cycle:

$$Q_{\mathrm{rev},i} \approx Q_{\mathrm{dis},i} \quad \text{(S10)}$$

The average reversible capacity over the first 100 cycles can then be approximated by the average discharge capacity:

$$\overline{Q}_{\mathrm{rev},100} \approx \overline{Q}_{\mathrm{dis},100} = \frac{\sum_{i=1}^{100} Q_{\mathrm{dis},i}}{100} \quad \text{(S11)}$$

It should be emphasized that this approximation is applied to each cycle within the first 100 cycles and is used to obtain the average per-cycle reversible capacity. It does not represent the cumulative amount of manganese participating over all cycles.

II. Calculation of the 100-Cycle-Averaged Apparent Cyclable Mn Inventory

When $\overline{Q}_{\mathrm{dis},100}$ is expressed in mAh g^{-1}, it can be converted into the average charge density in C g^{-1}:

$$\overline{Q}_{C,100} = 3.6 \times \overline{Q}_{\mathrm{dis},100} \quad \text{(S12)}$$

where the factor 3.6 converts mAh to C. According to Faraday's law, the average number of moles of electrons involved per gram of initially loaded β-MnO_2 is:

$$\overline{n}_{e,100} = \frac{\overline{Q}_{C,100}}{F} \quad \text{(S13)}$$

where F is the Faraday constant, 96485 C mol^{-1}. Since the MnO_2/Mn^{2+} conversion is a two-electron reaction, the 100-cycle-averaged apparent amount of manganese involved in reversible cycling can be estimated as:

$$\bar{n}_{\mathrm{Mn,app,100}} = \frac{\bar{Q}_{C,100}}{2F} = \frac{3.6 \times \bar{Q}_{\mathrm{dis,100}}}{2F}$$

(S14)

After converting mol g^{-1} to mmol g^{-1}, the equation becomes:

$$\bar{n}_{\mathrm{Mn,app,100}}\ (\mathrm{mmol\ Mn\ g^{-1}}) = 0.01865 \times \bar{Q}_{\mathrm{dis,100}}\ (\mathrm{mAh\ g^{-1}})$$

(S15) Equivalently, using the total discharge capacity over the first 100 cycles:

$$\bar{n}_{\mathrm{Mn,app,100}}\ (\mathrm{mmol\ Mn\ g^{-1}}) = 0.01865 \times \frac{Q_{\mathrm{dis,total,100}}}{100}$$

(S16)

Here, $\bar{n}_{\mathrm{Mn,\ app,100}}$ is defined as the 100-cycle-averaged capacity-derived apparent cyclable Mn inventory, normalized to the mass of the initially loaded β-MnO_2 active material. It should be emphasized that $Q_{\mathrm{dis,\ total,100}}$ is used only to calculate the average per-cycle discharge capacity, rather than to represent the cumulative amount of manganese participating over all cycles.

III. Calculation Results

Table S3 summarizes the total discharge capacity over the first 100 cycles, the corresponding average discharge capacity, and the calculated 100-cycle-averaged apparent cyclable Mn inventory for different electrolyte systems.

Table S3. 100-cycle-averaged capacity-derived apparent cyclable Mn inventory calculated from the average discharge capacity over the first 100 cycles.

Electrolyte system	Sum of discharge capacities over first 100 cycles / mAh g^{-1}	Average discharge capacity over first 100 cycles / mAh g^{-1}	100-cycle-averaged apparent cyclable Mn inventory / mmol Mn g^{-1}
$ZnSO_4$ + $C_6H_8O_7$ + $MnSO_4$	21096.2	210.962	3.93
$ZnSO_4$ + $Mn(CH_3COO)_2$	20677.0	206.770	3.86
$Zn(CH_3COO)_2$	2648.6	26.486	0.49
$ZnSO_4$	15948.5	159.485	2.97

IV. Discussion

The $ZnSO_4$ + $C_6H_8O_7$ + $MnSO_4$ electrolyte exhibits the highest 100-cycle-averaged apparent cyclable Mn inventory of 3.93 mmol Mn g^{-1}. This result indicates that the $C_6H_8O_7$-containing electrolyte provides the best average retention of cyclable manganese inventory over the first 100 cycles, which is consistent with its superior cycling stability. This improvement is attributed to proton regulation and suppression of ZSH-related side reactions, which help preserve active manganese species during prolonged cycling.

The $ZnSO_4$ + $Mn(CH_3COO)_2$ electrolyte also shows a high 100-cycle-averaged apparent cyclable Mn inventory of 3.86 mmol Mn g^{-1}, indicating enhanced reversible manganese utilization through Mn^{2+} supply and acetate-assisted MnO_2 deposition. However, this value is slightly lower than that of the $C_6H_8O_7$-containing electrolyte because the $Mn(CH_3COO)_2$ system delivers a high peak capacity but still undergoes capacity fading during extended cycling.

In contrast, the $Zn(CH_3COO)_2$ electrolyte exhibits the lowest value of 0.49 mmol Mn g^{-1}, consistent

with the suppressed MnO_2 reduction caused by proton consumption in the isolated acetate system. The $ZnSO_4$ electrolyte shows an intermediate value of 2.97 mmol Mn g^{-1}, but its average cyclable manganese inventory is limited by residual ZSH-related side reactions under the present testing conditions.

Overall, this 100-cycle-averaged capacity-derived analysis provides a more representative semi-quantitative comparison of the Mn-equivalent amount involved in reversible cycling over a fixed cycle window. These values should not be interpreted as direct measurements of the actual manganese inventory, but as discharge-capacity-derived electrochemical estimates of the average apparent cyclable Mn inventory during the first 100 cycles.

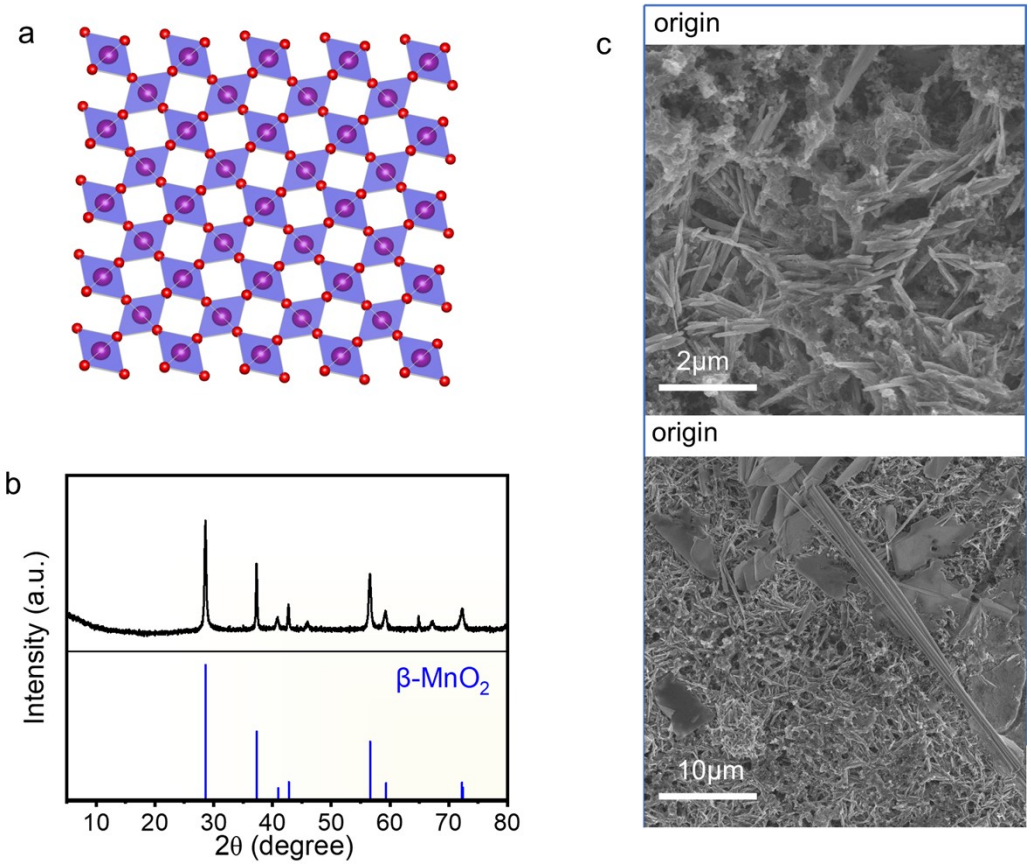

Fig. S1 (a) Crystal structure of β-MnO_2 showing one-dimensional tunnel lattice; (b) XRD pattern of β-MnO_2; (c) SEM images of β-MnO_2 at 5k and 10k magnifications.

As shown in Fig. S1(a), β-MnO_2 exhibits a one-dimensional tunnel-like lattice structure, which endows it with a high theoretical capacity and favorable ion conduction potential. The XRD pattern (Fig. S1(b)) is consistent with the standard pattern, confirming the crystalline phase purity of the material. The SEM images (Fig. S1(c)) illustrate the micromorphological characteristics of β-MnO_2.

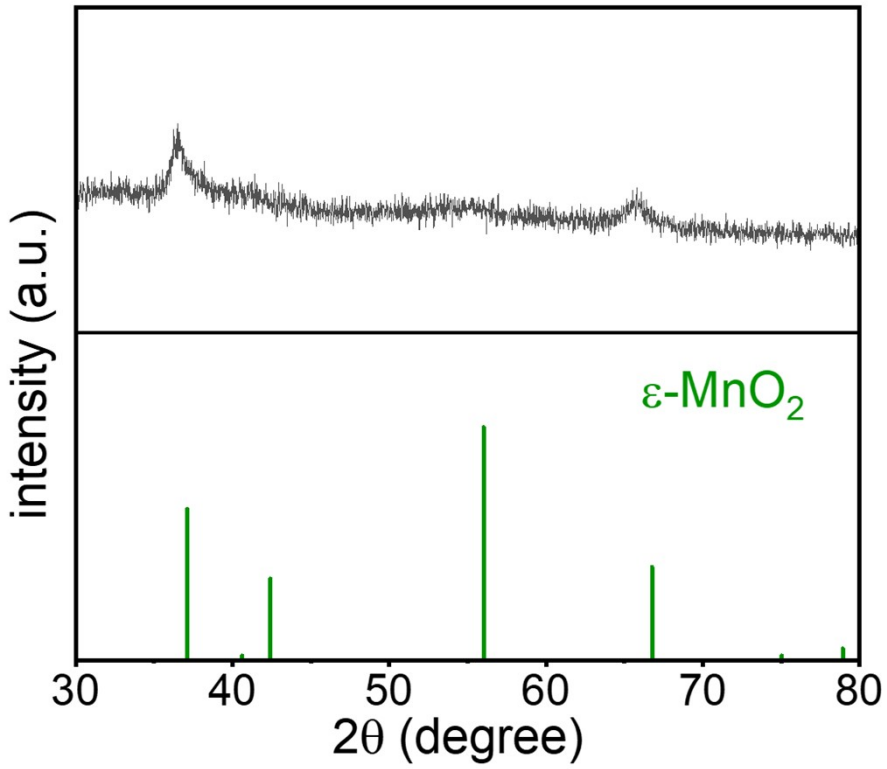

Fig. S2. XRD pattern of the accumulated deposits collected from repeated Mn^{2+} electrodeposition on Ti foil in the $ZnSO_4$ + $MnSO_4$ electrolyte.

To identify the phase of the deposits formed during the charging process, Mn^{2+} electrodeposition was performed on a Ti foil current collector. Since the amount of deposited material generated during a single charging process was insufficient for reliable XRD characterization, repeated deposition–collection cycles were conducted to accumulate sufficient deposits for phase analysis. After each deposition cycle, the deposited product was collected from the Ti foil, and the procedure was repeated multiple times.

As shown in Fig. S2, the XRD pattern of the accumulated deposits exhibits diffraction peaks consistent with those of ε-MnO_2. Although the diffraction peaks are relatively broad and weak due to the limited crystallinity and small amount of deposited material, the observed peak positions agree well with the characteristic reflections of ε-MnO_2 reported in the literature. These results indicate that ε-MnO_2 is the dominant phase formed during the charging process, providing additional evidence for the phase assignment of the deposits observed in Figs. 1c, 2b, and 3c of the main text.

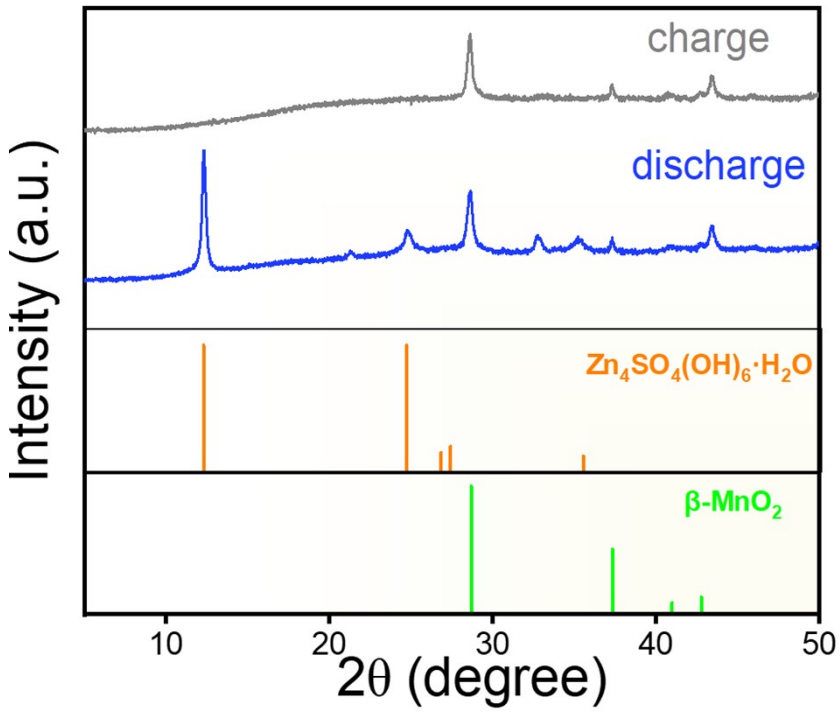

Fig. S3 XRD patterns of the $ZnSO_4$ electrolyte system after discharge to 0.9 V and after charge to 1.8 V.

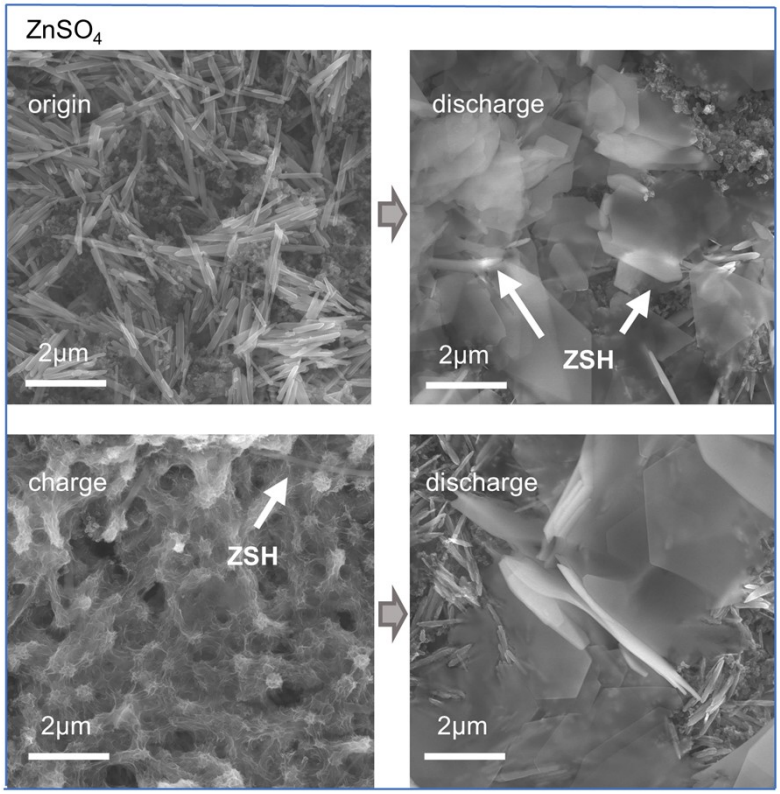

Fig. S4 SEM images of the $ZnSO_4$ electrolyte system: pristine cathode, after discharge to 0.9 V, after charge to 1.8 V and after discharge to 0.9 V.

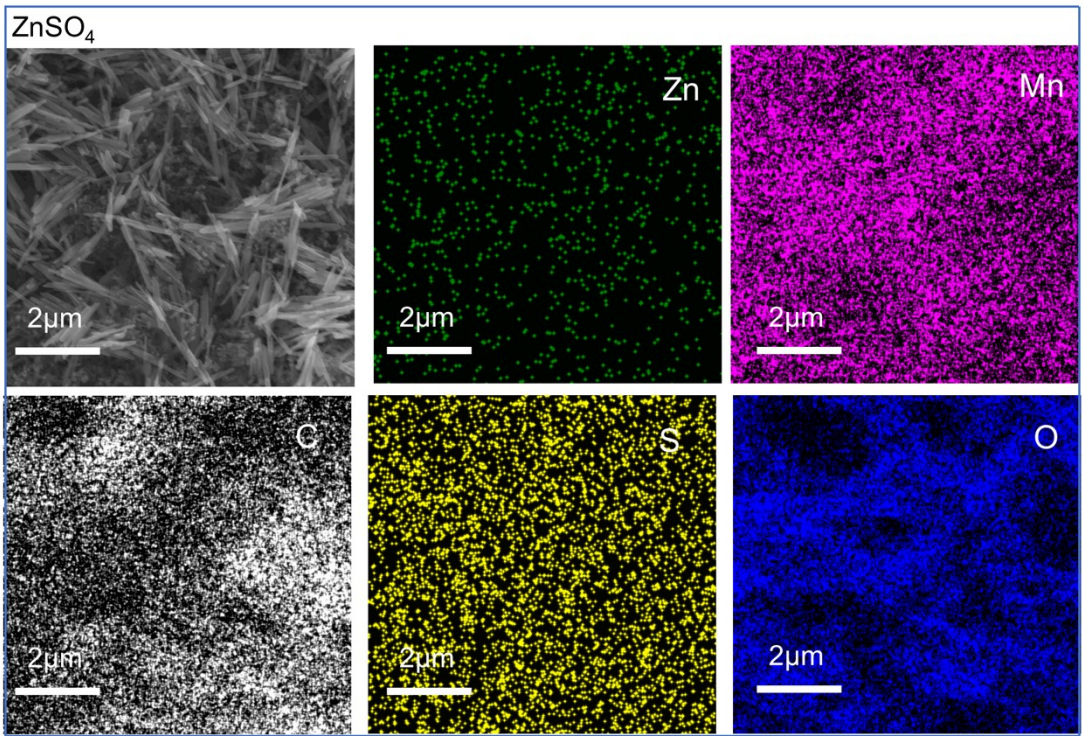

Fig. S5 EDS elemental maps (Zn, S, Mn, O, C) of the pristine cathode.

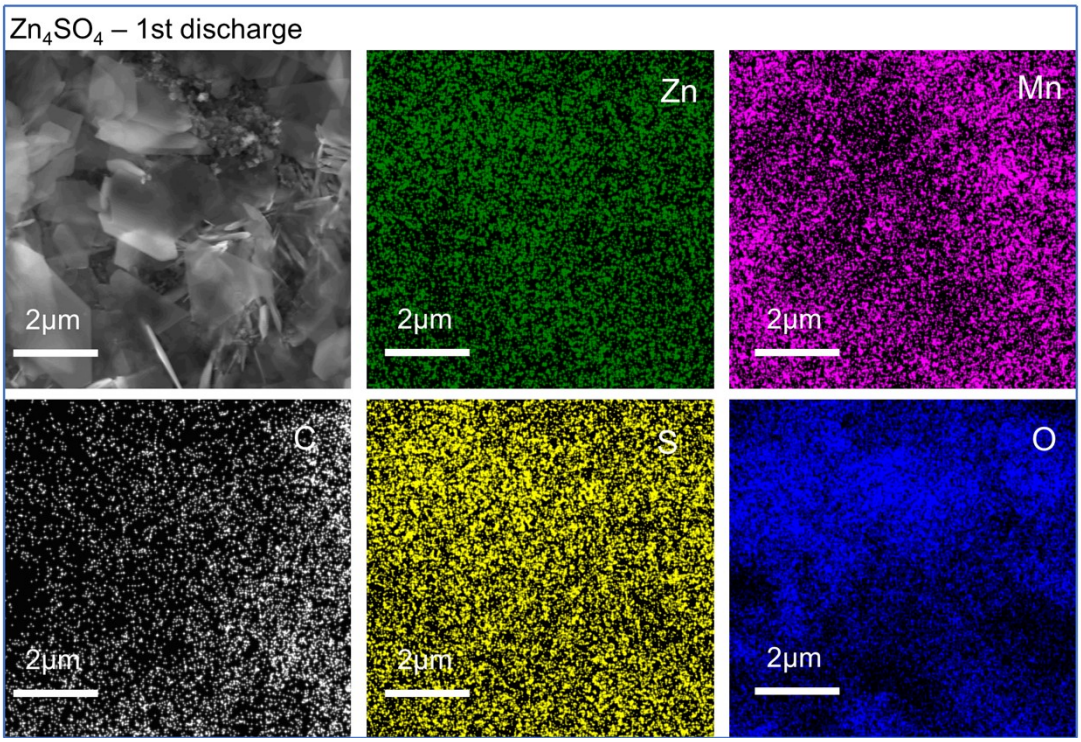

Fig. S6 EDS elemental maps (Zn, S, Mn, O, C) of the cathode after the first discharge to 0.9 V.

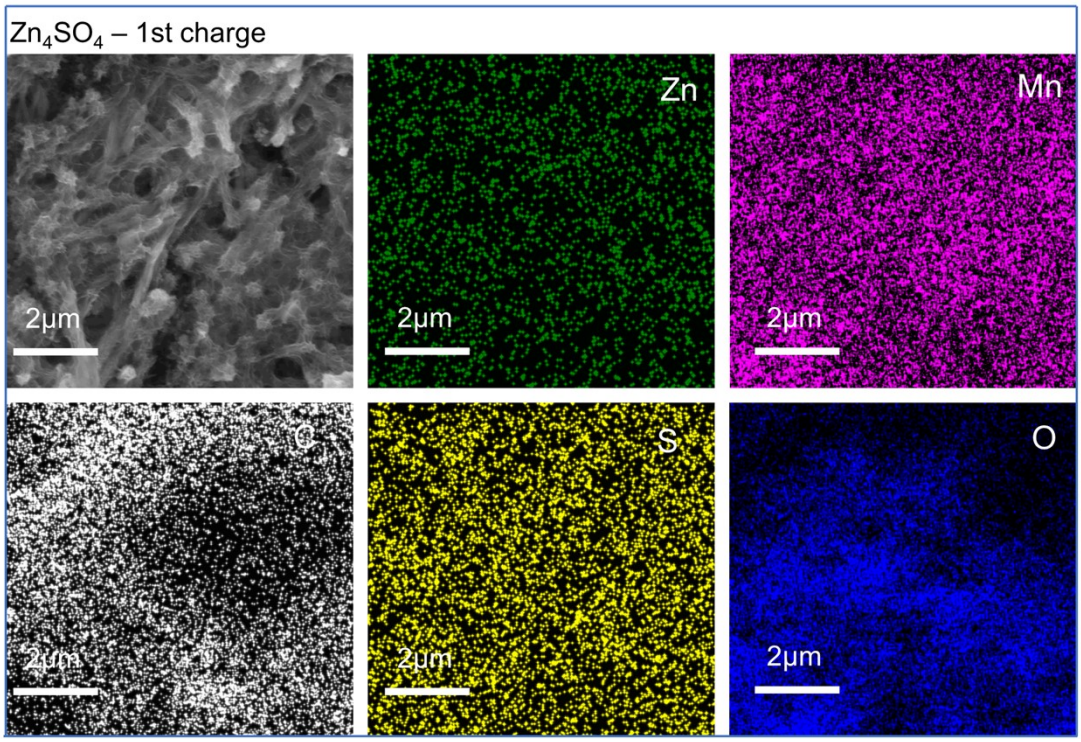

Fig. S7 EDS elemental maps (Zn, S, Mn, O, C) of the cathode after charge to 1.8 V.

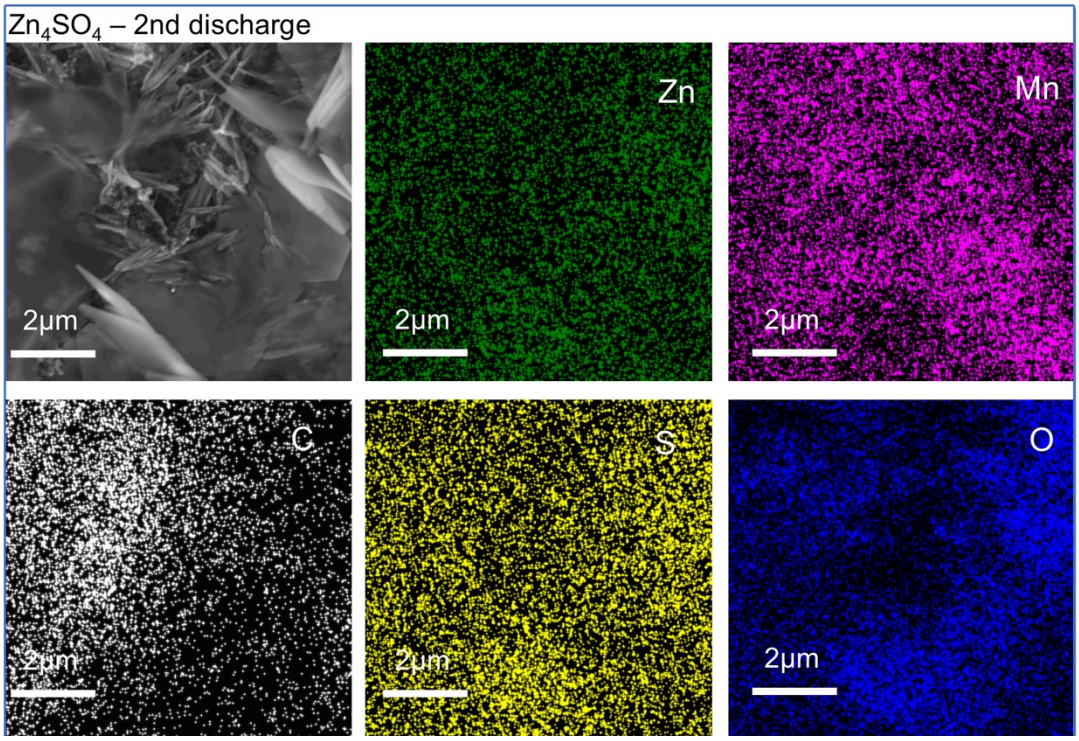

Fig. S8 EDS elemental maps (Zn, S, Mn, O, C) of the cathode after the second discharge to 0.9 V.

To further analyze the evolution behavior of the cathode interface in $ZnSO_4$-based electrolytes, we performed XRD and SEM characterization of the electrodes at different charge/discharge states. As shown in Fig. S3, after discharging to 0.9 V, diffraction peaks corresponding to basic zinc sulfate (ZSH) appear. After subsequent charging to 1.8 V, these diffraction peaks are still detectable, indicating that under our experimental conditions, the ZSH formed during discharge is not completely eliminated after charging and some residue remains. To unambiguously identify the deposit formed on the cathode after discharge and to distinguish it from regenerated MnO_2, energy-dispersive X-ray spectroscopy (EDS) was performed, as shown in Fig. S5–S8. After discharge, a clear increase in the characteristic signals of Zn and S (the latter corresponding to SO_4^{2-}) was observed, indicating the accumulation of ZSH on the electrode surface. Importantly, after subsequent charging, the Zn and S signals remained notably higher than those of the pristine electrode, suggesting that a portion of the ZSH formed during discharge persists after charging under the present experimental conditions.

It should be noted that this result does not imply that ZSH is irreversible in all $ZnSO_4$-based aqueous batteries[1-2]. Previous studies have shown that under specific mildly acidic $ZnSO_4$ electrolytes, appropriate voltage windows, and suitable electrode systems, the precipitation and dissolution of ZSH can exhibit good reversibility. The reversibility of ZSH is influenced by multiple factors, including the electrolyte composition, cathode material, operating voltage range, current density, and the local pH environment at the electrode/electrolyte interface[3-4].

In the present work, we employed a β-MnO_2 cathode and a $ZnSO_4$-based electrolyte with a voltage window of 0.9–1.8 V. During discharge, the reduction of MnO_2 continuously consumes H^+, leading to local alkalinization near the cathode surface and thereby promoting the formation of ZSH. This reaction can be expressed as[5-6]:

$$4Zn^{2+} + 7H_2O + SO_4^{2-} \rightarrow Zn_4SO_4(OH)_6 \cdot H_2O + 6H^+ \quad \text{(S17)}$$

The residual ZSH after charging may cover part of the active surface, hindering the complete conversion of MnO_2/Mn^{2+} and thereby reducing the cyclable manganese inventory available for subsequent cycles.

References

[1] Z. Wang, Y. Fang, J. Shi, Z. Ma, X. Qu and P. Li, *Adv. Energy Mater.*, 2024, **14**, 2303739.

[2] V. R. Kankanallu, X. Zheng, C. Lo, A. Kiss, E. Musterman, A. Pattammattel, A. C. Marschilok, E. S. Takeuchi, K. J. Takeuchi, X. Huang, M. Ge and Y. K. Chen-Wiegart, *J. Mater. Chem. A*, 2025, **13**, 1240.

[3] J. Huang, B. He, J. Zhi, P. Chen, C. Wang, H. Chen and X. S. Zhao, *J. Power Sources*, 2024, **623**, 235409.

[4] Q. Wang, Z. Zhang, Z. Hu, W. Du, Y. Zhang, M. Ye, Z. Wen, Y. Tang, X. Liu and C. C. Li, *Angew. Chem., Int. Ed.*, 2025, **64**, e202420772.

[5] Cheng, F. Y.; Chen, J.; Gou, X. L.; Shen, P. W. High-Power Alkaline Zn–MnO_2 Batteries Using γ-MnO_2 Nanowires/Nanotubes and Electrolytic Zinc Powder. Adv. Mater. 2005, **17 (22)**, 2753.

[6] Hu, Y. S.; Kienle, L.; Guo, Y. G.; Maier, J. High Lithium Electroactivity of Nanometer-Sized Rutile TiO_2. Adv. Mater. 2006, **18 (11)**, 1421.